AGU ADVANCING EARTH AND SPACE SCIENCE

Geophysical Research Letters®

RESEARCH LETTER
10.1029/2021GL096215

Bathymetry Beneath the Amery Ice Shelf, East Antarctica, Revealed by Airborne Gravity

Junjun Yang[1], Jingxue Guo[2], Jamin S. Greenbaum[3], Xiangbin Cui[2], Liangcheng Tu[1,4], Lin Li[2], Lenneke M. Jong[5], Xueyuan Tang[2], Bingrui Li[2], Donald D. Blankenship[6], Jason L. Roberts[5], Tas van Ommen[5], and Bo Sun[2]

[1]Institute of Geophysics, PGMF and School of Physics, Huazhong University of Science and Technology, Wuhan, China, [2]Polar Research Institute of China, Shanghai, China, [3]Scripps Institution of Oceanography, University of California, San Diego, La Jolla, CA, USA, [4]TianQin Research Center for Gravitational Physics, School of Physics and Astronomy, Sun Yat-sen University, Zhuhai, China, [5]Australian Antarctic Division, Kingston, TAS, Australia, [6]Institute for Geophysics, University of Texas at Austin, Austin, TX, USA

Abstract The bathymetry under the Amery Ice Shelf steers the flow of ocean currents transporting ocean heat, and thus is a prerequisite for precise modeling of ice-ocean interactions. However, hampered by thick ice, direct observations of sub-ice-shelf bathymetry are rare, limiting our ability to quantify the evolution of this sector and its future contribution to global mean sea level rise. We estimated the bathymetry of this region from airborne gravity anomaly using simulated annealing. Unlike the current model which shows a comparatively flat seafloor beneath the calving front, our estimation results reveal a 255-m-deep shoal at the western side and a 1,050-m-deep trough at the eastern side, which are important topographic features controlling the ocean heat transport into the sub-ice cavity. The new model also reveals previously unknown depressions and sills that are critical to an improved modeling of the sub-ice-shelf ocean circulation and induced basal melting.

Plain Language Summary The ocean currents are strongly steered by the seafloor topography. Therefore, the seafloor topography should be represented at fine resolution to study how the warm water melts the ice shelf from below. However, the seafloor beneath the largest ice shelf in East Antarctica remains poorly known, because the thick floating ice blocks direct bathymetric observations. We used gravity measured by airplane to infer the shape of the seafloor beneath the floating ice. The gravity-inferred seafloor topography model is substantially improved over the existing BedMachine Antarctica model, and reveals previously unknown topographic features. The newly identified seafloor topographic features could improve our knowledge about how much ocean heat enters the sub-ice cavity and how the ocean currents flow beneath the ice shelf. With this knowledge, scientists could more accurately project the response of the Amery Ice Shelf to ocean forcing and this region's future contribution to global mean sea level rise.

1. Introduction

The Amery Ice Shelf (AmIS) is the largest embayed ice shelf in East Antarctica. It is fed by the Lambert-Mellor-Fisher tributary glacial systems on the southernmost grounding line, and by MacRobertson Land and American Highland on its flanks (Figure 1a; Mouginot et al., 2017a). The catchments feeding the AmIS drain about 1.4 million km^2 in area (including the AmIS; Mouginot et al., 2017b) and hold enough ice to raise sea level by 7.8 m (Rignot et al., 2019). Recent studies (e.g., Depoorter et al., 2013; Pritchard et al., 2012; Rignot et al., 2013; Smith et al., 2020) found that increased basal melting of ice shelves has contributed to almost half of Antarctic coastal ice loss, through reduced buttressing of the glaciers feeding them. The southern AmIS has the deepest Antarctic ice in contact with the ocean, making it particularly susceptible to ocean heat since the in-situ melting point of ice decreases with increasing pressure. Sophisticated modeling of ice-ocean interactions (Galton-Fenzi et al., 2012; Gong et al., 2014; Liu et al., 2017; Williams et al., 2001) is needed for a better understanding of this sector's future evolution and its contribution to global mean sea level rise in a changing climate.

Seafloor topography steers the ocean circulation in the cavity under the AmIS (De Rydt et al., 2014), making it a fundamental boundary condition for modeling the response of the AmIS to ocean forcing, where higher accuracy and resolution lead to improved model performance (Goldberg et al., 2020). Troughs that provide pathways for warm modified Circumpolar Deep Water (mCDW) (Greenbaum et al., 2015; Liu et al., 2018; St-Laurent et al., 2013) should be identified and resolved, as well as sills in the seabed that isolate ice shelf cavities from

J. Guo and J. Yang contributed equally to this study.

Key Points:

- The seafloor topography beneath the Amery Ice Shelf, East Antarctica, is estimated from airborne gravity using simulated annealing
- Estimation results present updated ice front geometry, an important factor controlling the ocean heat transport into sub-ice cavity
- The model reveals previously unknown depressions at the western flank that are critical to an improved modeling of ocean circulation

Supporting Information:

Supporting Information may be found in the online version of this article.

Correspondence to:

J. Guo,
guojingxue@pric.org.cn
J. Yang
yang.741@osu.edu

Citation:

Yang, J., Guo, J., Greenbaum, J. S., Cui, X., Tu, L., Li, L., et al. (2021). Bathymetry beneath the Amery Ice Shelf, East Antarctica, revealed by airborne gravity. *Geophysical Research Letters*, *48*, e2021GL096215. https://doi.org/10.1029/2021GL096215

Received 22 SEP 2021
Accepted 11 DEC 2021

Author Contributions:

Conceptualization: Junjun Yang, Liangcheng Tu, Bo Sun
Data curation: Jingxue Guo, Jamin S. Greenbaum, Xiangbin Cui, Lin Li, Xueyuan Tang
Formal analysis: Junjun Yang
Funding acquisition: Junjun Yang, Jingxue Guo, Liangcheng Tu, Bo Sun
Investigation: Junjun Yang, Jingxue Guo, Jamin S. Greenbaum, Xiangbin Cui, Lenneke M. Jong
Methodology: Junjun Yang
Project Administration: Liangcheng Tu, Bo Sun
Resources: Jingxue Guo, Jamin S. Greenbaum, Xiangbin Cui, Lin Li, Xueyuan Tang

Software: Junjun Yang
Supervision: Liangcheng Tu, Bo Sun
Validation: Junjun Yang
Visualization: Junjun Yang
Writing – original draft: Junjun Yang
Writing – review & editing: Jamin S. Greenbaum

inflow (Rignot et al., 2016; Schaffer et al., 2020; Williams et al., 2001). However, traditional shipborne multibeam surveys are unavailable in regions covered by ice shelves. The seafloor topography under the AmIS, with an area of ~60,500 km^2, thus remains poorly known (Craven et al., 2004; Galton-Fenzi et al., 2008), limiting our ability to accurately reproduce the pattern and intensity of ice shelf melt using ice-ocean models.

In 2015, China launched a campaign to survey East Antarctica with the "Snow Eagle 601" aerogeophysical platform on which a gravimeter, radio-echo sounder, and laser altimeter are configured and integrated (Cui et al., 2020). During the campaign, key north-south lines and dense east-west lines over the AmIS were flown (Figure 1a). This study uses these data to estimate the bathymetry beneath the AmIS through a global optimization method called simulated annealing and discusses the potential impact of the topographic features identified in the new bathymetric model on the ocean circulation beneath the AmIS.

2. Data and Methods

2.1. Airborne Gravity

Airborne gravity was measured by the Polar Research Institute of China (PRIC) in January 2018 using the GT-2A airborne gravimeter (e.g., Greenbaum et al., 2015) mounted on a BT-67 fixed-wing aircraft named Snow Eagle 601 (Cui et al., 2020). Survey altitude ranged from 103 to 2,351 m to maintain a nominal range of 600 m above the surface on all flights. The airplane flew at speeds of about 300 km/hr with line spacing ranging from 11 to 26 km. The data acquisition rate of the gravimeter was set to 2 Hz. The raw gravity measurements were corrected for the kinematic accelerations of the airplane and the Eötvös effects using carrier-based differential GPS. A latitude correction, computed using the International Gravity Formula 1980, and a free-air correction, computed using the second-order formula for the GRS80 ellipsoid (Hinze et al., 2013), were applied to yield free-air gravity anomalies; note that this quantity is known as the "gravity disturbance" in geodesy literature (Hackney & Featherstone, 2003). Next, the free-air gravity anomalies were filtered with a 150 s full-wavelength low-pass filter to suppress noise, corresponding to an along-track resolution of 6.25 km. Data noise of the final gravity product was 1 mGal. Data gaps between flight lines were interpolated from the filtered gravity using a minimum curvature method (Smith & Wessel, 1990).

2.2. Laser Altimeter and Ice-Penetrating Radar Data

The BT-67 airplane was equipped with a Riegl LD90-3800-HiP laser altimeter to measure the ice surface elevation (Figure 1b) and a phase-coherent ice-penetrating radar (Cui et al., 2020) to derive the ice bottom elevation (Figure 1c) along the flight tracks. The crossover differences of the ice surface elevation data are -0.7 ± 4.1 m. The crossover differences of the ice bottom elevation data are -3.1 ± 73.0 m. At places not covered by airplane measurements, the ice surface and ice bottom elevations were obtained from the Reference Elevation Model of Antarctica (REMA; Howat et al., 2019) and BedMachine Antarctica v2 (BMA; Morlighem et al., 2020), respectively. The accuracy of the REMA elevation is better than 1 m while the accuracy of BMA elevation is about 100 m in this region. The geometry of the ice layer was used to forward compute the gravity anomalies due to the ice layer and to define the upper search limit of the unknown seafloor topography. Bedrock elevations constrained by ice-penetrating radar data were also used to estimate the regional gravity field (Section 2.4.2).

2.3. Hydrographic Data

To analyze the water masses abutting the AmIS, two hydrographic data sets are used in this study. The first consists of Conductivity, Temperature, Depth (CTD) data along the calving front of the AmIS (see the solid yellow circles in Figure 1a) collected from February 28, 2012, to March 4, 2012, during the 28th Chinese National Antarctic Research Expedition (CHINARE). The second data set consists of a moored time series of temperature and salinity recorded from February 2003 to February 2005 at the hot-water-drilled borehole AM02 (see the black pentagram in Figure 1a). The mooring data were obtained by the Amery Ice Shelf Ocean Research project (Craven et al., 2004), which used a hot water drill to deploy CTD sensors to three depths (335, 556, and 761 m) to acquire hydrographic data beneath the AmIS. The shallowest sensor is positioned 12 m below the ice shelf base.

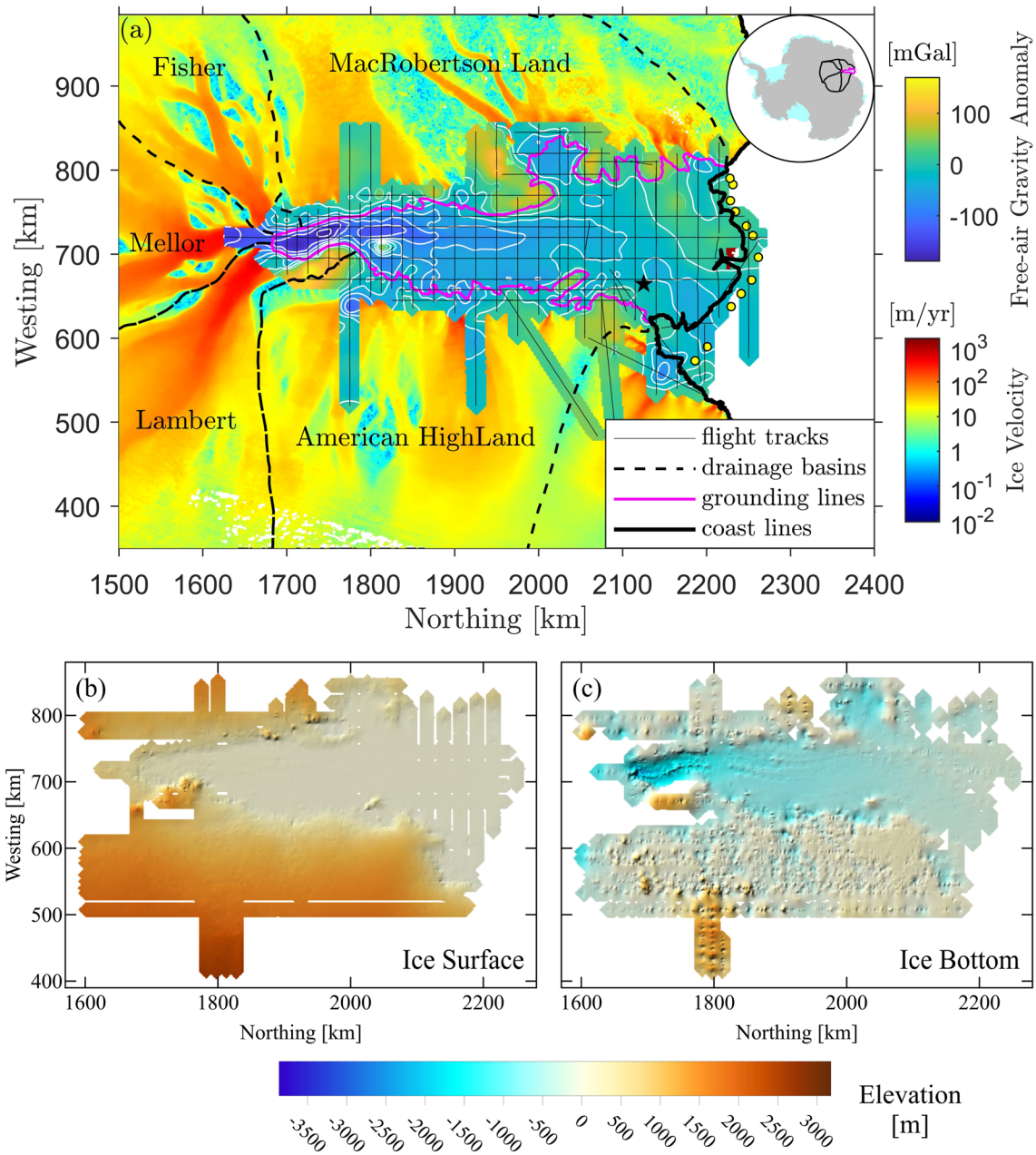

Figure 1. (a) Free-air gravity anomalies measured by Snow Eagle 601 (color coded using the upper color bar) overlain on a map of ice velocity from 2016 to 2017 (color coded using the lower color bar). The white lines above the gravity anomalies are contours with 30 mGal interval, and the thin black lines are flight trajectories. The dashed black lines delineate drainage basins. The magenta lines represent the grounding lines. The thick black lines are the coast/calving front boundary. The inset indicates the locations of the AmIS (magenta) and surrounding drainage basins (black). Solid yellow circles represent CTD stations. The black pentagram is the borehole position. (b) Ice surface elevation measured by laser altimeter. (c) Ice bottom elevation derived from ice-penetrating radar measurements. These maps use the polar stereographic projection with the true scale at 71°S, origin 90°S, 0°E. The reference ellipsoid is Hughes 1980.

2.4. Gravity Inversion

The measured gravity anomalies at flight altitude integrate the gravitational effects of the density difference between the seafloor topography and the overlying water and/or ice layers, the density variations within the shallow subsurface, and the regional isostatic compensation (Watts, 2001) at the Mohorovicic discontinuity (Yang, Luo, Tu, et al., 2020). The latter two effects are not due to the seafloor topography and should be removed prior to the inversion. We assume a uniform bedrock density throughout this study, remove the gravitational effect of the ice layer and the regional gravity field from the measured gravity anomalies, and use the remaining gravity anomaly

to estimate the seafloor topography through the simulated annealing method (Ingber, 1989; Uzun et al., 2020) by minimizing the difference between the remaining and the forward-computed gravity anomalies.

2.4.1. Forward Model

To forward compute the gravity anomaly from the geometry of mass layers, the volume of the study area was discretized into adjacent right rectangular prisms (RRPs) with horizontal dimensions of 12×12 km^2 over the ice shelf, and 500×500 m^2 everywhere else. The model domain contains three layers with densities of 0.917 g/cm^3 for ice (Morlighem et al., 2020), 1.0277 g/cm^3 for ocean water, and 2.67 g/cm^3 for bedrock. The identity of each prism was determined using the land classification mask inside the BMA model. The x and y coordinates of the RRPs were known during discretization. The upper and lower boundary of an RRP represents one of the following surfaces: Earth's surface, ice bottom, and seafloor. The elevation of the Earth's surface and the ice bottom were obtained through data and methods described in Section 2.2. Seafloor topography directly beneath the AmIS and covered by airborne gravity was treated as an unknown parameter to be estimated through simulated annealing. Seafloor topography in areas not surveyed with the aircraft was interpolated from BMA. The gravitational effect of one RRP can be computed using Nagy et al. (2000)'s formula. The gravity anomaly at each computation point is the sum of the gravitational effect of the near zone prisms, that is, prisms within a horizonal distance of 100 km from this point.

2.4.2. Removal of the Non-Terrain Effects

Ice shelves not in hydrostatic equilibrium and grounded ice produce gravity anomalies that are not generated by seafloor topography (Cochran et al., 2014). Besides, the lithospheric plate flexes under various loads (e.g., mountains), causing long-wavelength regional gravity anomalies (Watts, 2001). These non-terrain effects should be removed from the gravity anomaly measurements prior to the inversion. The gravity anomalies at flight altitude generated by the ice layer were computed using the RRP model described in Section 2.4.1. The regional gravity was estimated using a technique frequently used in recent studies (An et al., 2019; Jordan et al., 2020; Millan et al., 2020; Yang, Luo, & Tu, 2020) that could also partially account for density variations within the shallow subsurface. That is, we calculate the difference between the measured and forward-computed gravity anomalies over ice-free land where the surface elevation was constrained by REMA model (Howat et al., 2019) and over grounded ice where the bedrock elevation was constrained by ice-penetrating radar data. Then this difference was interpolated into areas without constraints using a minimum curvature method (Smith & Wessel, 1990) with the results treated as the estimated regional gravity. The non-terrain effects, namely the gravity due to the ice layer and the estimated regional gravity, were removed from the measured free-air gravity anomaly. The remaining gravity anomaly (hereinafter referred to as *pseudo-observed gravity anomaly*) was used to estimate the seafloor topography using simulated annealing.

2.4.3. Simulated Annealing

Simulated annealing is a stochastic search method useful for solving global optimization problems (Kirkpatrick et al., 1983) and can be applied to nonlinear inversion problems with large dimensions. In the case of this study, it iteratively searches over the parameter space of the unknown seafloor topography; the upper and lower search limits are defined as the bottom of the ice layer and 1.5 km below the BMA-interpolated seafloor topography, respectively. The gravity anomalies at flight altitude are forward computed from the seafloor topography and compared with the pseudo-observed gravity anomalies in each iteration. The *cost function*, defined as the average of the squared differences between the forward-computed and pseudo-observed gravity anomalies, is computed to quantitatively evaluate their difference. During the iterations, the simulated annealing gradually converges to an optimal seafloor topography that minimizes the cost function. Interested readers are referred to recent literature (e.g., Yang et al., 2018) for an overview of the simulated annealing algorithm.

3. Results

3.1. New Bathymetric Model

The simulated annealing program was assigned 64 CPU cores from a supercomputer, ran for 3.3 h, and exited after 1×10^7 iterations. During the iterations, the cost function decreases as the iteration number increases (Figure S1a in Supporting Information S1), dropping more than 2 orders of magnitude during the annealing process, and reaching 4.28 mGal^2 at the end of the iteration. The mean and standard deviation of the differences between the

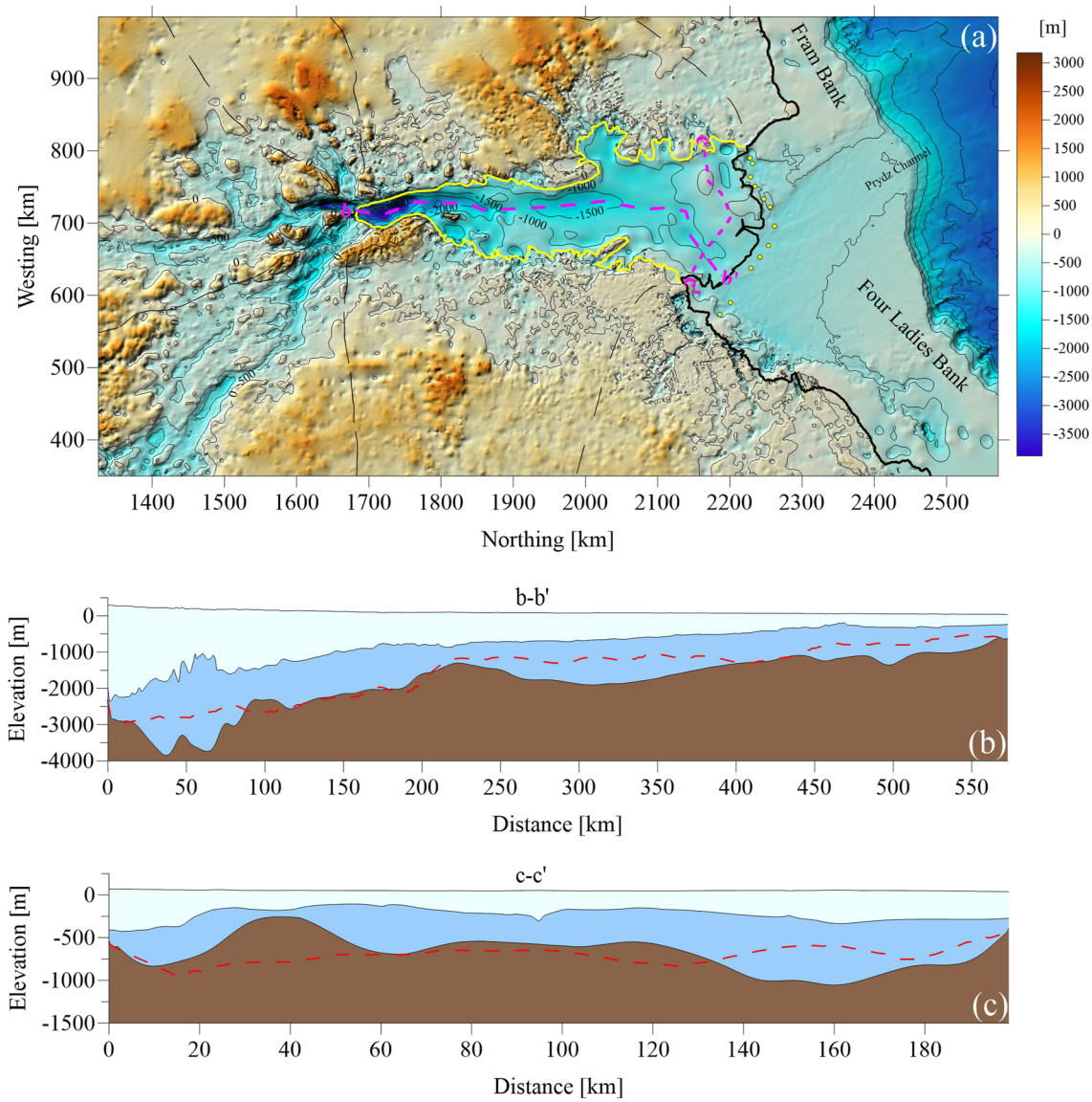

Figure 2. (a) New seafloor topography inverted from airborne gravity anomalies (inside the yellow line) and bed elevation from BedMachine Antarctica v2 model (outside the yellow line). Thin black lines are contours with 500 m interval. The yellow lines are grounding lines. The thick black lines are the coast/calving front boundary. The black dashed lines delineate drainage basins. The yellow circles represent CTD measurements. Profiles along the magenta dashed lines b-b' and c-c' are shown in (b) and (c), respectively. In the lower two panels, the light cyan layers are the ice shelf, the blue layer is ocean water, and the brown layer is bedrock. The red dashed lines are the seafloor depths interpolated from the bed elevation in BedMachine Antarctica v2. All heights in this figure are meters above the EIGEN-6C4 geoid.

pseudo-observed gravity anomalies and the one forward computed from the gravity-estimated seafloor topography (Figure S1b in Supporting Information S1) are −0.2 and 2.1 mGal, respectively. This gravity misfit and the 1 mGal uncertainty in gravity data translate into a nominal root-mean-square error of 62 m in bed elevation if we use a conversion factor of 5 mGal per 100 m of water (An et al., 2019; Constantino et al., 2020; Millan et al., 2020). In comparison, the mean and standard deviation of the differences computed using the seafloor topography in BMA model (Figure S1c in Supporting Information S1) are 6.9 and 17.5 mGal, respectively. Note that the nominal accuracy of 62 m is a best-case value, provided the uniform bedrock density assumption holds. The actual half-wavelength resolution of the seafloor topography as estimated from airborne gravity was 12 km, but for consistency with BMA, the estimation result was interpolated onto a 500 × 500 m^2 grid using a cubic interpolation algorithm (Yang, 1986). The new seafloor topography model estimated from pseudo-observed gravity anomaly is shown in Figure 2a. It reveals topographic features smaller than those resolvable in previously published models (e.g., BMA, Figure S2 in Supporting Information S1).

The area from the calving front of the AmIS to 80 km inland features a 40-km-wide sill on the west and a 65-km-wide trough on the east. The magenta dashed line c-c′ in Figure 2a delineates the location of the bed profile shown in Figure 2c that extends parallel to the calving front but lies 40 km further inland. The seafloor drops from 550 m deep at point c to 830 m deep at km 10, indicating a 20 km wide trough on the westernmost side. The seafloor becomes shallower eastward, until reaches a 255 m deep ridge at km 38. In the following 90 km, most of the seafloor depth ranges from 540 to 690 m. After km 125, the seafloor gradually deepens to more than 1,050 m over the following 20 km and remains around this depth for about 20 km. Then the seafloor rises to 820 m deep at km 180, before shoaling again to 400 m at km 198.

As shown in profile b-b′ (Figure 2b), the bed slope beneath the AmIS generally deepens inland, with two small sills present in the southern part. The seafloor depth around point b′ is 590 m. It deepens to the southwest, with seafloor depths ranging between 1,010 m to 1,355 m in the following 130 km along b′-b. After km 440, the seafloor deepens southward, reaching 1,900 m deep at km 310. Then it becomes shallower southward, until reaching a 1,300 m deep sill at km 223. After km 223, the seafloor deepens gently to the south until reaching 2,565 m near km 117 before a 15 km wide sill is found at a depth of 2,300 m near km 100. The seafloor then deepens sharply to more than 3,700 m at the southernmost end.

3.2. Water Masses Arriving at the AmIS

The source of ocean heat to the AmIS is mCDW, carried by the alongshore Antarctic Slope Current (Whitworth et al., 1998) and entering this sector from the east through dynamic effects of key submarine troughs (Liu et al., 2017, 2018). The ocean circulation beneath the AmIS has been modeled by several studies (e.g., Galton-Fenzi et al., 2012; Williams et al., 2001), which suggest a cyclonic circulation featuring inflow of shelf waters in the east and outflow of Ice Shelf Water (ISW) in the west. Presenting an updated modeling of the sub-ice-shelf ocean circulation and the associated basal melting based on the gravity-inferred bathymetric model is beyond the scope of this study. In this section, we show the presence of ocean heat by analyzing the properties of the water masses arriving at the AmIS. Then in Section 4, the potential impact of the topographic features identified in the new bathymetric model on the ocean circulation beneath the AmIS is discussed.

Vertical sections of temperature and salinity (Figures 3a and 3b) derived from CTD measurements collected during the 28th CHINARE are used to identify the water masses arriving at the calving front of the AmIS in the austral summer. Warm Antarctic Surface Water (AASW, Liu et al., 2018) with temperature >-0.4°C and salinity <34.3 psu is identified at the eastern flank of the calving front (km [2,241, 652] in Figure 2a), but is confined to the upper layer (<150 m depth). Cold continental Shelf Water (SW, Liu et al., 2017) with temperature <-1.8°C and salinity >34.4 psu occupies the majority of the water columns deeper than 200 m, with an exception at the western flank where ISW with temperature lower than the surface freezing point of -1.89°C (Herraiz-Borreguero et al., 2016) is identified at the layer right beneath the AASW. The *ocean thermal forcing*, defined as the difference between the potential temperature and pressure-dependent freezing point (Morlighem et al., 2019), is calculated (Figure 3c). Due to the rapid decline of the freezing point with depth (Fujino et al., 1974), the ocean thermal forcing below 200 m increases with depth, reaching 0.8°C at 1 km depth. So, the observed SW is capable of melting the deep ice and drives the formation of ISW. Since the seafloor beneath the AmIS deepens southward, larger ocean thermal forcing is expected at the southern region of the AmIS (Yu et al., 2010).

The arrival of mCDW in austral winter is inferred from the moored time series of temperature and salinity at the hot-water-drilled borehole AM02, which have been analyzed by several studies (e.g., Herraiz-Borreguero et al., 2015). These mooring records (Figures 3d and 3e) show seasonal variability due to changes in the inflow of the water masses. In February, the layer adjacent to the uppermost sensor is occupied by cold ISW of similar characteristics to the ISW shown in Figure 3a. Starting from March, warm mCDW enters the AmIS cavity, melts the ice shelf base, and drives the formation of ISW (Herraiz-Borreguero et al., 2015). The progressively enhancing inflow of mCDW leads to warmer and fresher waters observed at the uppermost sensor at AM02. The temperature peaks in June. Then it decreases as the inflow of mCDW is exhausted, until reaching the in-situ freezing point of -2.14°C in September.

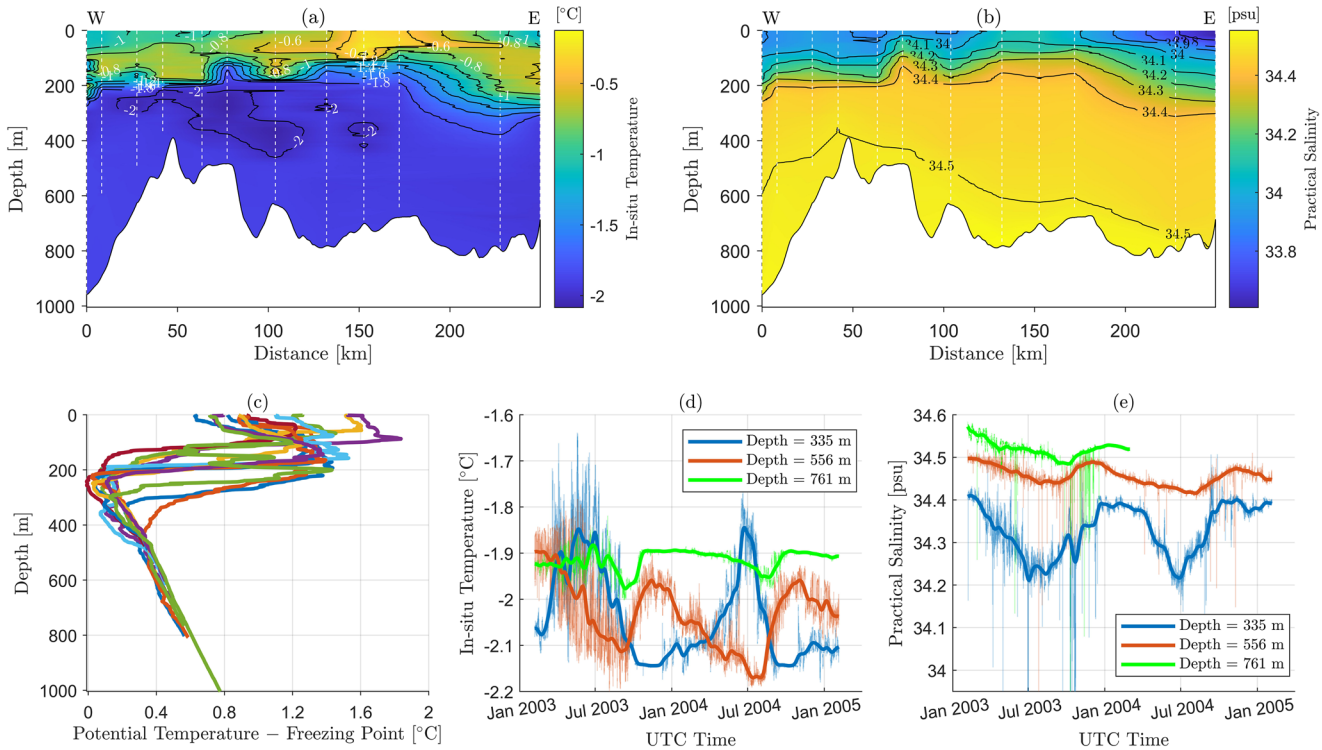

Figure 3. (a) In-situ ocean temperature vertical section along the calving front of the AmIS derived from the CTDs shown in Figure 2a. The distance axis corresponds to the slice going from west to east. CTD locations are indicated with white dashed lines. The black lines are contours with 0.2°C interval. The white area at the bottom represents the seafloor. (b) Practical salinity vertical section overlaid by contours with 0.1 psu interval. (c) Profiles of ocean thermal forcing (the difference between the potential temperature of the ocean and the freezing point of seawater). (d) In-situ temperature and (e) salinity time series at three depths derived from CTD moorings at hot-water-drilled borehole AM02 shown in Figure 1a. The thin lines in (d) and (e) are the unfiltered records while the overlying thick lines are records filtered through a Gaussian low-pass filter with cutoff wavelength of 30 days.

4. Discussion

4.1. Topographic Steering of Ocean Currents

As emphasized by Williams et al. (2001) and Schodlok et al. (2016), the ocean circulation beneath the AmIS is generally steered by the geometry of the sub-ice-shelf cavity. We calculated the thickness of the water column (TWC) by subtracting the seafloor elevation from the ice bottom elevation derived from ice-penetrating radar. Differences are found between the TWC computed using gravity-inferred seafloor topography and the one computed using seafloor topography inside the BMA model (Figure 4). First, on the eastern flank near the calving front (i.e., between km [2,080, 710] and km [2,200, 650]), Figure 4a shows a thicker water column, facilitating the intrusion of mCDW. Bed profile c-c' in Figure 2c provides another perspective to the seafloor near the ice front. It shows that the current BMA model presents a comparatively flat seafloor topography, whereas the gravity-inferred seafloor topography reveals a trough at the eastern side and a ridge at the western side. As Wåhlin et al. (2020) found that the depth-independent (barotropic) component (typically the dominant component) of the heat flow toward an ice shelf could be diverted by an abrupt change in the thickness of the water column at ice shelf fronts, the newly identified ice front geometry has the potential to markedly change the heat flux entering the sub-ice cavity in future modeling studies. Second, in the middle of the AmIS, a thick water column is identified over the western flank (Figure 4a), which is not shown in the BMA model (Figure 4b). Its location is consistent with a S-shaped ice bottom fracture shown in Figure 1c that naturally extends from the southernmost to the middle of the AmIS. This thick water column serving as water channel may lead to updated knowledge about ocean current paths and associated ocean heat distribution. Near km [1,900, 715], the water column is thin, and thus acts as a barrier controlling the southward flowing of seawater (Schaffer et al., 2020). Near km [1,870, 740] and km [1,850, 700], Figure 4a does not show thick water columns as Figure 4b does. To the south of km 1,770, the gravity-inferred seafloor is about 900 m deeper than the BMA model. These newly identified topographic

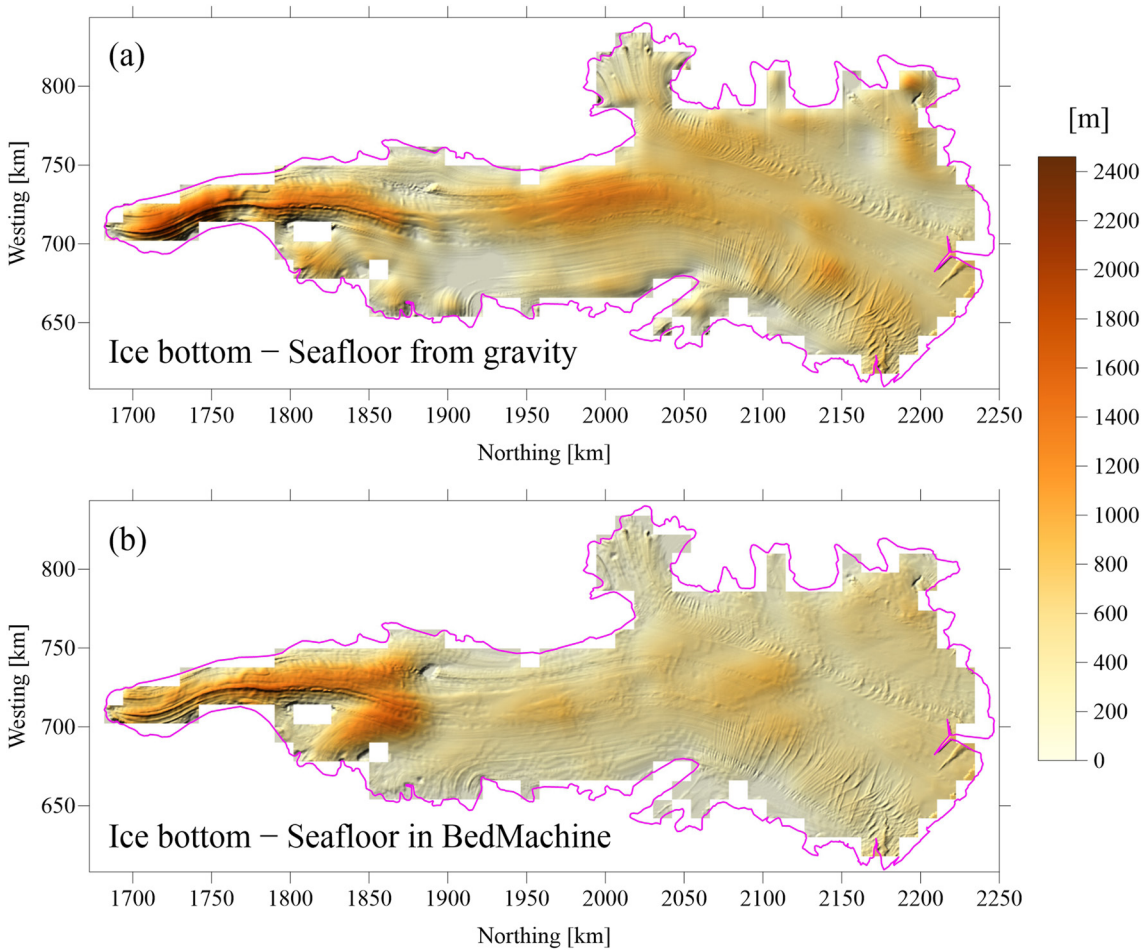

Figure 4. The thickness of the water column in the sub-ice-shelf cavity. (a) Difference between the ice bottom elevation derived from ice-penetrating radar and the seafloor topography estimated from airborne gravity. (b) Difference between the ice bottom elevation and the seafloor topography in BedMachine Antarctica v2 model. The magenta lines delineate the boundary of the Amery Ice Shelf.

features are critical to an improved modeling of the ocean circulation and associated basal melting beneath the AmIS (Galton-Fenzi et al., 2012; Liu et al., 2017; Schodlok et al., 2016).

5. Conclusions

The AmIS is the third-largest embayed ice shelf in Antarctica, buttressing the largest drainage basin in East Antarctica with 7.8 m of sea level potential. Although it has been observed to be stable in recent years (King et al., 2009; Tong et al., 2018), its southern region has the deepest Antarctic ice in contact with the ocean, making it particularly susceptible to the warming trends in the seawater adjacent to Antarctica (Schmidtko et al., 2014; Williams et al., 2002). To advance our understanding of its future contribution to global mean sea level rise in a warming climate, it is necessary to numerically simulate and project the sub-ice-shelf ocean circulation and the associated basal melting, which requires precise bathymetry as a boundary condition (Catania et al., 2018; Fox-Kemper et al., 2021). However, direct observations of the seafloor depths are sparse beneath the AmIS. We present a new seafloor topography map of this region indirectly inferred from dense airborne gravity anomalies through simulated annealing. With a half-wavelength resolution of 12 km, the new bathymetric model reveals topographic features that are not resolvable in previously published models such as BedMachine Antarctica v2, which are critical to reliable estimates of the submarine melting processes (Jourdain et al., 2020). With the refined seafloor topography model, we anticipate an improved performance in modeling the response of the AmIS to ocean forcing.

Data Availability Statement

The gravity-inferred seafloor topography model is available at this link (http://doi.org/10.5281/zenodo.5651609) and is available upon request to J. Yang (yang.741@osu.edu). It is in NetCDF format and can be read through MATLAB command "ncread." The hot-water-drilled borehole data are available at this link (https://data.aad.gov.au/metadata/records/ASAC_1164). The ship-lowered CTD data collected during the 28th CHINARE (https://www.chinare.org.cn/en/metadata/35a77e6d-b75a-40b5-9569-bfb66e2e4032) and the airborne geophysical data (https://www.chinare.org.cn/en/metadata/8971b431-d7df-471c-8f9d-4554e89b3040) are publicly available at Chinese National Arctic and Antarctic Data Center.

Acknowledgments
The authors are thankful to Chengyan Liu for providing valuable discussions. Comments from the editor, Mathieu Morlighem, and two anonymous reviewers were highly appreciated as they led to a significant improvement of the original manuscript. Computations were partially supported by National Supercomputer Center in Guangzhou. This study was partially supported by grants (42006197, 41876227, 41874089, and 41941007) from the National Natural Science Foundation of China and a grant (SKLGED2020-1-1-E) from State Key Laboratory of Geodesy and Earth's Dynamics. J.S.G was supported by NSF grant NSF OPP-2114454. L.M.J., J.L.R., and T.v.O. acknowledge grants (AAS 4346 and 4511) from the Australian Antarctic Division. D.D.B. acknowledges support from the G. Unger Vetlesen Foundation.

References

An, L., Rignot, E., Chauche, N., Holland, D., Holland, D., Jakobsson, M., et al. (2019). Bathymetry of southeast Greenland from Ocean Melting Greenland (OMG) data. *Geophysical Research Letters*, *46*(20), 11197–11205. https://doi.org/10.1029/2019gl083953

Catania, G. A., Stearns, L. A., Sutherland, D. A., Fried, M. J., Bartholomaus, T. C., Morlighem, M., et al. (2018). Geometric controls on tidewater glacier retreat in central western Greenland. *Journal of Geophysical Research: Earth Surface*, *123*(8), 2024–2038. https://doi.org/10.1029/2017JF004499

Cochran, J. R., Jacobs, S. S., Tinto, K. J., & Bell, R. E. (2014). Bathymetric and oceanic controls on Abbot Ice Shelf thickness and stability. *The Cryosphere*, *8*(3), 877–889. https://doi.org/10.5194/tc-8-877-2014

Constantino, R. R., Tinto, K. J., Bell, R. E., Porter, D. F., & Jordan, T. A. (2020). Seafloor depth of George VI Sound, Antarctic Peninsula, from inversion of aerogravity data. *Geophysical Research Letters*, *47*(21), e2020GL088654. https://doi.org/10.1029/2020gl088654

Craven, M., Allison, I., Brand, R., Elcheikh, A., Hunter, J., Hemer, M., & Donoghue, S. (2004). Initial borehole results from the Amery Ice Shelf hot-water drilling project. *Annals of Glaciology*, *39*, 531–539. https://doi.org/10.3189/172756404781814311

Cui, X., Jeofry, H., Greenbaum, J. S., Guo, J., Li, L., Lindzey, L. E., et al. (2020). Bed topography of Princess Elizabeth Land in East Antarctica. *Earth System Science Data*, *12*(4), 2765–2774. https://doi.org/10.5194/essd-12-2765-2020

Depoorter, M. A., Bamber, J. L., Griggs, J. A., Lenaerts, J. T. M., Ligtenberg, S. R. M., van den Broeke, M. R., & Moholdt, G. (2013). Calving fluxes and basal melt rates of Antarctic ice shelves. *Nature*, *502*(7469), 89–92. https://doi.org/10.1038/nature12567

De Rydt, J., Holland, P. R., Dutrieux, P., & Jenkins, A. (2014). Geometric and oceanographic controls on melting beneath Pine Island Glacier. *Journal of Geophysical Research: Oceans*, *119*(4), 2420–2438. https://doi.org/10.1002/2013jc009513

Fox-Kemper, B., Hewitt, H. T., Xiao, C., Aðalgeirsdóttir, G., Drijfhout, S. S., Edwards, T. L., et al. (2021). Ocean, cryosphere and sea level change. In V. Masson-Delmotte, P. Zhai, A. Pirani, S. L. Connors, C. Péan, S. Berger, et al. (Eds.), Climate change 2021: The physical science basis. *Contribution of working group I to the sixth assessment report of the intergovernmental panel on climate change* (pp. 55–56). Cambridge University Press.

Fujino, K., Lewis, E. L., & Perkin, R. G. (1974). The freezing point of seawater at pressures up to 100 bars. *Journal of Geophysical Research*, *79*(12), 1792–1797. https://doi.org/10.1029/JC079i012p01792

Galton-Fenzi, B. K., Hunter, J. R., Coleman, R., Marsland, S. J., & Warner, R. C. (2012). Modeling the basal melting and marine ice accretion of the Amery Ice Shelf. *Journal of Geophysical Research: Oceans*, *117*, C09031. https://doi.org/10.1029/2012JC008214

Galton-Fenzi, B. K., Maraldi, C., Coleman, R., & Hunter, J. (2008). The cavity under the Amery Ice Shelf, East Antarctica. *Journal of Glaciology*, *54*(188), 881–887. https://doi.org/10.3189/002214308787779898

Goldberg, D. N., Smith, T. A., Narayanan, S. H. K., Heimbach, P., & Morlighem, M. (2020). Bathymetric influences on Antarctic Ice-Shelf melt rates. *Journal of Geophysical Research: Oceans*, *125*(11), e2020JC016370. https://doi.org/10.1029/2020JC016370

Gong, Y., Cornford, S. L., & Payne, A. J. (2014). Modelling the response of the Lambert Glacier–Amery Ice Shelf system, East Antarctica, to uncertain climate forcing over the 21st and 22nd centuries. *The Cryosphere*, *8*(3), 1057–1068. https://doi.org/10.5194/tc-8-1057-2014

Greenbaum, J. S., Blankenship, D. D., Young, D. A., Richter, T. G., Roberts, J. L., Aitken, A. R. A., et al. (2015). Ocean access to a cavity beneath Totten Glacier in East Antarctica. *Nature Geoscience*, *8*(4), 294–298. https://doi.org/10.1038/ngeo2388

Hackney, R. I., & Featherstone, W. E. (2003). Geodetic versus geophysical perspectives of the 'gravity anomaly'. *Geophysical Journal International*, *154*(1), 35–43. https://doi.org/10.1046/j.1365-246X.2003.01941.x

Herraiz-Borreguero, L., Church, J. A., Allison, I., Pena-Molino, B., Coleman, R., Tomczak, M., & Craven, M. (2016). Basal melt, seasonal water mass transformation, ocean current variability, and deep convection processes along the Amery Ice Shelf calving front, East Antarctica. *Journal of Geophysical Research: Oceans*, *121*(7), 4946–4965. https://doi.org/10.1002/2016jc011858

Herraiz-Borreguero, L., Coleman, R., Allison, I., Rintoul, S. R., Craven, M., & Williams, G. D. (2015). Circulation of modified Circumpolar Deep Water and basal melt beneath the Amery Ice Shelf, East Antarctica. *Journal of Geophysical Research: Oceans*, *120*(4), 3098–3112. https://doi.org/10.1002/2015jc010697

Hinze, W. J., Von Frese, R. R. B., & Saad, A. H. (2013). *Gravity and magnetic exploration: Principles, practices, and applications*. Cambridge University Press.

Howat, I. M., Porter, C., Smith, B. E., Noh, M. J., & Morin, P. (2019). The reference elevation model of Antarctica. *The Cryosphere*, *13*(2), 665–674. https://doi.org/10.5194/tc-13-665-2019

Ingber, L. (1989). Very fast simulated re-annealing. *Mathematical and Computer Modelling*, *12*(8), 967–973. https://doi.org/10.1016/0895-7177(89)90202-1

Jordan, T. A., Porter, D., Tinto, K., Millan, R., Muto, A., Hogan, K., et al. (2020). New gravity-derived bathymetry for the Thwaites, Crosson, and Dotson ice shelves revealing two ice shelf populations. *The Cryosphere*, *14*(9), 2869–2882. https://doi.org/10.5194/tc-14-2869-2020

Jourdain, N. C., Asay-Davis, X., Hattermann, T., Straneo, F., Seroussi, H., Little, C. M., & Nowicki, S. (2020). A protocol for calculating basal melt rates in the ISMIP6 Antarctic ice sheet projections. *The Cryosphere*, *14*(9), 3111–3134. https://doi.org/10.5194/tc-14-3111-2020

King, M. A., Coleman, R., Freemantle, A.-J., Fricker, H. A., Hurd, R. S., & Legrésy, B., et al. (2009). A 4-decade record of elevation change of the Amery Ice Shelf, East Antarctica. *Journal of Geophysical Research: Earth Surface*, *114*, F01010. https://doi.org/10.1029/2008JF001094

Kirkpatrick, S., Gelatt, C. D., & Vecchi, M. P. (1983). Optimization by simulated annealing. *Science*, *220*(4598), 671–680. https://doi.org/10.1126/science.220.4598.671

Liu, C., Wang, Z., Cheng, C., Wu, Y., Xia, R., Li, B., & Li, X. (2018). On the modified Circumpolar Deep Water upwelling over the Four Ladies bank in Prydz Bay, East Antarctica. *Journal of Geophysical Research: Oceans*, *123*(11), 7819–7838. https://doi.org/10.1029/2018JC014026

Liu, C., Wang, Z., Cheng, C., Xia, R., Li, B., & Xie, Z. (2017). Modeling modified Circumpolar Deep Water intrusions onto the Prydz Bay continental shelf, east Antarctica. *Journal of Geophysical Research: Oceans*, *122*(7), 5198–5217. https://doi.org/10.1002/2016JC012336

Millan, R., St-Laurent, P., Rignot, E., Morlighem, M., Mouginot, J., & Scheuchl, B. (2020). Constraining an ocean model under Getz Ice Shelf, Antarctica, using a gravity-derived bathymetry. *Geophysical Research Letters*, *47*(13), e2019GL086522. https://doi.org/10.1029/2019gl086522

Morlighem, M., Rignot, E., Binder, T., Blankenship, D., Drews, R., Eagles, G., et al. (2020). Deep glacial troughs and stabilizing ridges unveiled beneath the margins of the Antarctic ice sheet. *Nature Geoscience*, *13*(2), 132–137. https://doi.org/10.1038/s41561-019-0510-8

Morlighem, M., Wood, M., Seroussi, H., Choi, Y., & Rignot, E. (2019). Modeling the response of northwest Greenland to enhanced ocean thermal forcing and subglacial discharge. *The Cryosphere*, *13*(2), 723–734. https://doi.org/10.5194/tc-13-723-2019

Mouginot, J., Scheuchl, B., & Rignot, E. (2017a). *MEaSUREs Annual Antarctic Ice Velocity Maps 2005-2017, Version 1*. NASA National Snow and Ice Data Center Distributed Active Archive Center. https://doi.org/10.5067/9T4EPQXTJYW9

Mouginot, J., Scheuchl, B., & Rignot, E. (2017b). *MEaSUREs Antarctic Boundaries for IPY 2007-2009 from Satellite Radar, Version 2*. NASA National Snow and Ice Data Center Distributed Active Archive Center. https://doi.org/10.5067/AXE4121732AD

Nagy, D., Papp, G., & Benedek, J. (2000). The gravitational potential and its derivatives for the prism. *Journal of Geodesy*, *74*(7–8), 552–560. https://doi.org/10.1007/s001900000116

Pritchard, H. D., Ligtenberg, S. R. M., Fricker, H. A., Vaughan, D. G., van den Broeke, M. R., & Padman, L. (2012). Antarctic ice-sheet loss driven by basal melting of ice shelves. *Nature*, *484*(7395), 502–505. https://doi.org/10.1038/nature10968

Rignot, E., Fenty, I., Xu, Y., Cai, C., Velicogna, I., Cofaigh, C. Ó., et al. (2016). Bathymetry data reveal glaciers vulnerable to ice-ocean interaction in Uummannaq and Vaigat glacial fjords, west Greenland. *Geophysical Research Letters*, *43*(6), 2667–2674. https://doi.org/10.1002/2016GL067832

Rignot, E., Jacobs, S., Mouginot, J., & Scheuchl, B. (2013). Ice-shelf melting around Antarctica. *Science*, *341*(6143), 266–270. https://doi.org/10.1126/science.1235798

Rignot, E., Mouginot, J., Scheuchl, B., van den Broeke, M., van Wessem, M. J., & Morlighem, M. (2019). Four decades of Antarctic Ice Sheet mass balance from 1979-2017. *Proceedings of the National Academy of Sciences of the United States of America*, *116*(4), 1095–1103. https://doi.org/10.1073/pnas.1812883116

Schaffer, J., Kanzow, T., von Appen, W.-J., von Albedyll, L., Arndt, J. E., & Roberts, D. H. (2020). Bathymetry constrains ocean heat supply to Greenland's largest glacier tongue. *Nature Geoscience*, *13*(3), 227–231. https://doi.org/10.1038/s41561-019-0529-x

Schmidtko, S., Heywood, K. J., Thompson, A. F., & Aoki, S. (2014). Multidecadal warming of Antarctic waters. *Science*, *346*(6214), 1227–1231. https://doi.org/10.1126/science.1256117

Schodlok, M. P., Menemenlis, D., & Rignot, E. J. (2016). Ice shelf basal melt rates around Antarctica from simulations and observations. *Journal of Geophysical Research: Oceans*, *121*(2), 1085–1109. https://doi.org/10.1002/2015JC011117

Smith, B., Fricker, H. A., Gardner, A. S., Medley, B., Nilsson, J., Paolo, F. S., et al. (2020). Pervasive ice sheet mass loss reflects competing ocean and atmosphere processes. *Science*, *368*(6496), 1239–1242. https://doi.org/10.1126/science.aaz5845

Smith, W. H. F., & Wessel, P. (1990). Gridding with continuous curvature splines in tension. *Geophysics*, *55*(3), 293–305. https://doi.org/10.1190/1.1442837

St-Laurent, P., Klinck, J. M., & Dinniman, M. S. (2013). On the role of coastal troughs in the circulation of warm circumpolar deep water on Antarctic shelves. *Journal of Physical Oceanography*, *43*(1), 51–64. https://doi.org/10.1175/jpo-d-11-0237.1

Tong, X., Liu, S., Li, R., Xie, H., Liu, S., Qiao, G., et al. (2018). Multi-track extraction of two-dimensional surface velocity by the combined use of differential and multiple-aperture InSAR in the Amery Ice Shelf, East Antarctica. *Remote Sensing of Environment*, *204*, 122–137. https://doi.org/10.1016/j.rse.2017.10.036

Uzun, S., Erkan, K., & Jekeli, C. (2020). Using gravity gradients to estimate fault parameters in the Wichita Uplift region. *Geophysical Journal International*, *222*(3), 1704–1716. https://doi.org/10.1093/gji/ggaa267

Wåhlin, A. K., Steiger, N., Darelius, E., Assmann, K. M., Glessmer, M. S., Ha, H. K., et al. (2020). Ice front blocking of ocean heat transport to an Antarctic ice shelf. *Nature*, *578*(7796), 568–571. https://doi.org/10.1038/s41586-020-2014-5

Watts, A. B. (2001). *Isostasy and flexure of the lithosphere*. Cambridge University Press.

Whitworth, T., III, Orsi, A. H., Kim, S.-J., Nowlin, W. D., Jr, & Locarnini, R. A. (1998). Water masses and mixing near the Antarctic slope front. In S. S. Jacobs, & R. F. Weiss (Eds.), *Ocean, ice, and atmosphere: Interactions at the Antarctic continental margin* (pp. 1–27). https://doi.org/10.1029/AR075p0001

Williams, M. J. M., Grosfeld, K., Warner, R. C., Gerdes, R., & Determann, J. (2001). Ocean circulation and ice-ocean interaction beneath the Amery Ice Shelf, Antarctica. *Journal of Geophysical Research*, *106*(C10), 22383–22399. https://doi.org/10.1029/2000jc000236

Williams, M. J. M., Warner, R. C., & Budd, W. F. (2002). Sensitivity of the Amery Ice Shelf, Antarctica, to changes in the climate of the Southern Ocean. *Journal of Climate*, *15*(19), 2740–2757. https://doi.org/10.1175/1520-0442(2002)015<2740:Sotais>2.0.Co;2

Yang, T. Y. (1986). *Finite element structural analysis*. Prentice Hall.

Yang, J., Jekeli, C., & Liu, L. (2018). Seafloor topography estimation from gravity gradients using simulated annealing. *Journal of Geophysical Research: Solid Earth*, *123*(8), 6958–6975. https://doi.org/10.1029/2018JB015883

Yang, J., Luo, Z., & Tu, L. (2020). Ocean access to Zachariæ Isstrøm glacier, northeast Greenland, revealed by OMG airborne gravity. *Journal of Geophysical Research: Solid Earth*, *125*(11), e2020JB020281. https://doi.org/10.1029/2020JB020281

Yang, J., Luo, Z., Tu, L., Li, S., Guo, J., & Fan, D. (2020). On the feasibility of seafloor topography estimation from airborne gravity gradients: Performance analysis using real data. *Remote Sensing*, *12*(24), 4092. https://doi.org/10.3390/rs12244092

Yu, J., Liu, H., Jezek, K. C., Warner, R. C., & Wen, J. (2010). Analysis of velocity field, mass balance, and basal melt of the Lambert Glacier–Amery Ice Shelf system by incorporating Radarsat SAR interferometry and ICESat laser altimetry measurements. *Journal of Geophysical Research*, *115*, B11102. https://doi.org/10.1029/2010jb007456

Geophysical Research Letters

Supporting Information for

Bathymetry beneath the Amery ice shelf, East Antarctica, revealed by airborne gravity

Junjun Yang[2,*], Jingxue Guo[1,*], Jamin S. Greenbaum[3], Xiangbin Cui[1], Liangcheng Tu[2,4], Lin Li[1], Lenneke M. Jong[5], Xueyuan Tang[1], Bingrui Li[1], Donald D. Blankenship[6], Jason L. Roberts[5], Tas van Ommen[5], and Bo Sun[1]

[1]Polar Research Institute of China, Shanghai 200136, China

[2]Institute of Geophysics, PGMF and School of Physics, Huazhong University of Science and Technology, Wuhan 430074, China

[3]Scripps Institution of Oceanography, University of California, San Diego, La Jolla, CA 92093, USA

[4]TianQin Research Center for Gravitational Physics, School of Physics and Astronomy, Sun Yat-sen University, Zhuhai 519082, China

[5]Australian Antarctic Division, Kingston, Tasmania 7050, Australia

[6]Institute for Geophysics, University of Texas at Austin, Austin, Texas 78758, USA

[*]J. Yang and J. Guo contributed equally to this work

Contents of this file

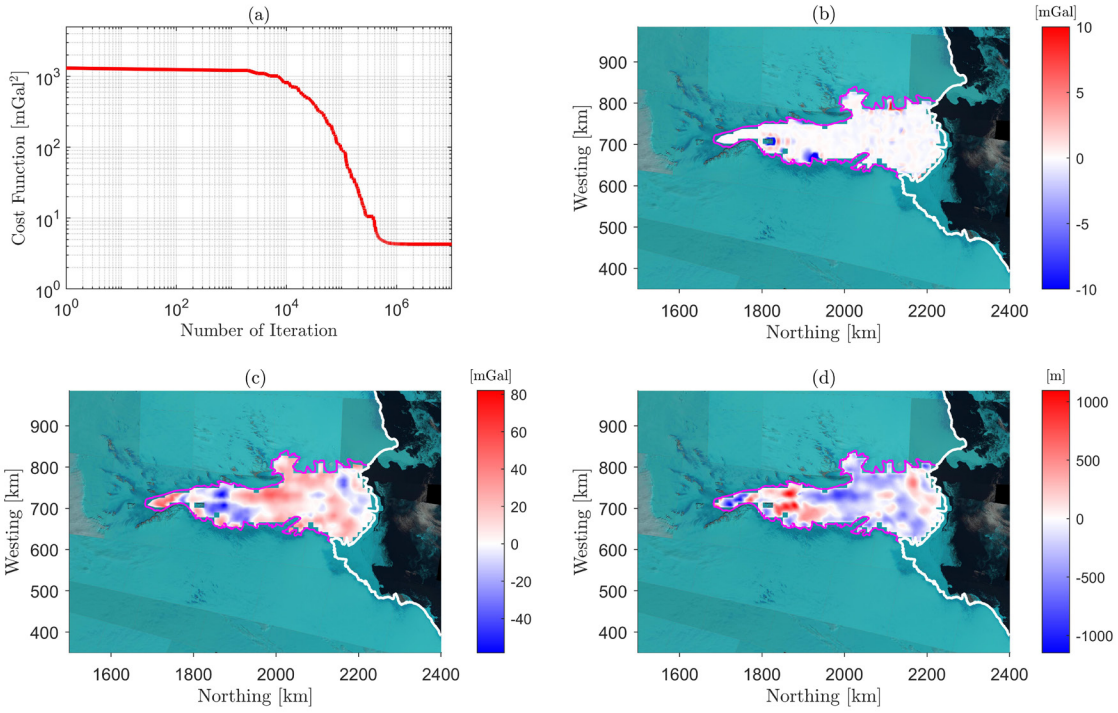

Figure S1. (a) The cost function decreases as the iteration number increases. (b) Differences between the pseudo-observed gravity anomalies and the one forward computed from the gravity-estimated seafloor topography. The white line is the coast/calving front boundary. The thin magenta line is grounding line. The background Landsat 8 image is acquired in January 2018. (c) Differences between the pseudo-observed gravity anomalies and the one forward computed from bed elevations in BedMachine Antarctica v2. (d) Differences between the gravity-estimated seafloor topography and BedMachine Antarctica v2.

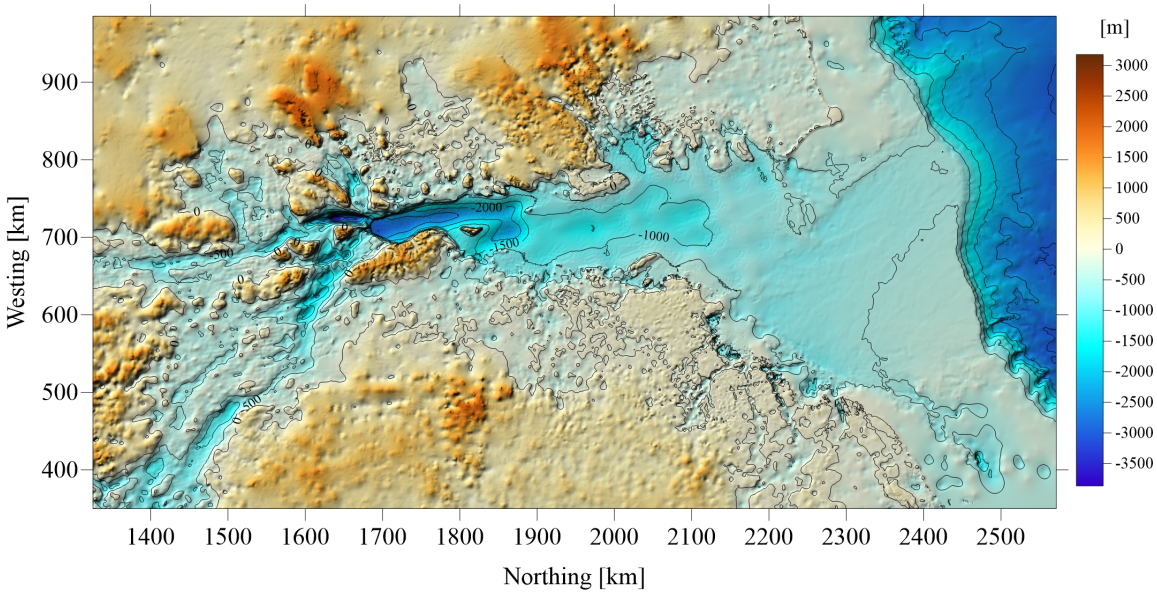

Figure S2. Bed elevations (orthometric height in meters referred to the EIGEN-6C4 geoid) around the Amery ice shelf from BedMachine Antarctica v2 model. Thin black lines are contours with 500 m interval.